Effect of the Atmospheric Stability Condition on Buoyant Plume Dynamics

Ritambhara Raj Dubey, Bikash Mahato, Neda Yaghoobian*

Florida State University, FAMU-FSU College of Engineering, Department of Mechanical Engineering, Tallahassee, FL, USA

Abstract

Buoyant plumes from various geophysical events significantly contribute to atmospheric pollution, affecting air quality, human health, and ecosystems. Understanding the dispersion dynamics of these plumes is essential for managing their environmental impacts and improving predictive models. Plume behavior is strongly influenced by the stability conditions of the atmospheric boundary layer, which vary between day and night due to diurnal changes in the Earth's surface temperature. During the daytime, solar heating creates an unstable boundary layer, often extending to several kilometers in height, while at night, radiative cooling leads to a stable boundary layer, typically a few hundred meters deep with weaker turbulence. Using large-eddy simulations, this study investigates how these diurnal variations in atmospheric stability affect the dynamics and dispersal behavior of turbulent plumes in crossflows. The results indicate that the plume's energy content and decay are highly influenced by the state of the atmospheric stratification, leading to distinctive patterns of dispersion, entrainment, and spread. By understanding the mechanisms governing the behavior of plumes, this study aims to contribute to better planning, management, and mitigation of their adverse effects.

Keywords: Atmospheric stratification; Buoyant plumes; Crossflow; Enstrophy; Inversion layer; LES

---

*Corresponding email address: nyaghoobian@eng.famu.fsu.edu

1. Introduction

Plumes are buoyant flows that arise when a less dense fluid, typically heated or chemically altered, ascends through a denser ambient medium. Turbulent buoyant plumes are prevalent in nature, arising from phenomena like wildland fires and prescribed burns, which release significant heat and particulate matter; volcanic eruptions, which discharge ash and gases; chimney smokestacks, which emit industrial pollutants; and sea ice melting, which drives plume formation in polar regions (e.g., Briggs, 1972; Carey & Bursik, 2015; Hewitt, 2020; Mallia & Kochanski, 2023; Potter, 2012; Price et al., 2016). These plumes play a significant role in the transport and dispersion of heat, moisture, and particulate matter within the atmosphere and oceans, potentially leading to substantial climatic and environmental consequences.

In the atmosphere, plumes that ascend into the troposphere can influence regional and global climates by altering atmospheric properties such as insolation and cloud microphysics (Andreae et al., 2004; Penner et al., 1992). Conversely, plumes confined to the atmospheric boundary layer can contribute to persistent temperature inversions (Robock, 1988), disrupt local air quality through unexpected dispersion patterns (Lareau & Clements, 2015), and pose health risks by introducing pollutants into the local environment (Larsen et al., 2018). A thorough understanding of plume dynamics in the atmosphere is essential for assessing air quality, planning effective responses, and informing public health advisories.

The study of buoyant plume dynamics has a long history, with early work primarily focusing on neutral environments. Morton et al. (1956) introduced the classical plume model, which established a link between the entrainment of ambient air and the plume's vertical velocity. Turner (1962, 1969) expanded this understanding by investigating the initiation of turbulent plumes and their mixing processes. These foundational studies laid the groundwork for understanding plume behavior in both neutral and quiescent conditions. While major plume dynamic studies are performed by considering neutral background conditions (Bhaganagar & Bhimireddy, 2020; Chen & Bhaganagar, 2023; Khan & Rao, 2023; Scase et al., 2006), fewer studies have explored plume behavior in stratified environments. Early studies on plumes in a stratified environment represented entrainment as a function of local Richardson numbers (Ellison & Turner, 1959; Priestley & Ball, 1955), treating it as a constant. However, later research revealed the unsteady nature of entrainment, varying with plume height and stratification conditions (Huq, 1997; Mukherjee et al., 2023).

Subsequent studies emphasized the complex behavior of plumes in stratified environments, showing that plume behavior is strongly influenced by factors such as buoyancy flux, momentum flux, and buoyancy frequency (Mirajkar & Balasubramanian, 2017). Golay (1982) observed that plume behavior in quiescent stably stratified conditions can be divided into two distinct phases: an initial phase where turbulence generated by the source dominates, followed by a phase where the background condition becomes the controlling factor. Devenish et al. (2010) reported a similar finding, noting that plumes in a quiescent stably stratified medium initially behave like those in a neutral environment until a certain height, beyond which the effects of stratification become significant. Once the plume reaches its maximum rise height in a stably stratified medium, it experiences damped oscillations (Contini et al., 2009). Later, Mirajkar and Balasubramanian (2017) observed that in stationary, stably stratified conditions the strength of stratification influences the plume's maximum and spreading height. These studies collectively demonstrate that, under quiescent conditions, plume growth, entrainment, and rise height are strongly influenced by the stable condition of the background flow. Although significant progress has been made in understanding plume behavior in neutral and stably stratified environments (Ashrafi et al., 2017; Bhaganagar & Bhimireddy, 2020; Diez et al., 2003; Khan & Rao, 2023; Meehan & Hamlington, 2023; M. Pham et al., 2007; Scase et al., 2006), further research is needed to explore the effects of varying atmospheric stability, particularly in turbulent, non-quiescent conditions.

Mass and heat dispersion in turbulent flows fundamentally depend on the characteristics of the carrying flow. Since real atmospheric conditions are rarely quiescent, plume development and contaminant dispersion in the atmosphere are similarly influenced by the nature of background turbulence (Matulka et al., 2014; Slawson & Csanady, 1971; Wright, 1994). Specifically relevant to plume dynamics, a recent study by Chung and Koseff (2023) highlighted that background flow structures, induced by canopy effects, can substantially alter buoyant plume dynamics by modifying their oscillatory behavior and entrainment patterns. A relevant question is whether similar effects arise in conditions where both background turbulence and stratification are present. Specifically, how background crossflow and stratification affect the initiation, dispersion, and evolution of plumes has yet to be fully explored. It should also be noted that comparative studies on plume dynamics under different stratified conditions are limited. In a study, mainly focusing on the usefulness of a numerical approach, Nakayama et al. (2014) investigated the spanwise and vertical plume dispersion under different atmospheric stability conditions. Their study indicated that the highest and lowest dispersions are, respectively, associated with unstable and stable conditions.

This study investigates the dynamics of buoyant turbulent plumes in non-quiescent environments with varying atmospheric stratification conditions. Using Large Eddy Simulations (LES), we explore how background turbulence modulates plume initiation, dispersion, and the evolution of both mean and turbulent properties. The rest of the paper is structured as follows: Sect. 2 describes the model used in this study and its validation, together with the simulation setup. In Sect. 3, the results discussing the background flow conditions, plume development and spread, mean plume characteristics, and energy distribution within the plume are presented, followed by a summary section.

2. Model Description and Simulation Setup

2.1. Model description

The computational modeling of the atmospheric turbulent flow and plumes therein in this work was performed using the LES technique. This study used the PALM model system (version 6.0) that was developed for investigating the atmospheric and oceanic flows (Maronga et al., 2015, 2020). Using PALM, the modeling of the turbulent flow was carried out by solving the non-hydrostatic, filtered continuity (Eq. 1) and Navier-Stokes (Eq. 2) equations under the Boussinesq approximation, together with the potential temperature (Eq. 3) and passive scalar (Eq. 4) equations to obtain the instantaneous filtered velocity components ($\overline{u_k}$), potential temperature ($\bar{\theta}$), and scalar concentration ($\bar{s}$).

$$\frac{\partial \overline{u_k}}{\partial x_k} = 0 \tag{1}$$

$$\frac{\partial \bar{u}_\imath}{\partial t} = -\frac{\partial \bar{u}_\imath \overline{u_k}}{\partial x_k} - \frac{1}{\rho_0}\frac{\partial \bar{\pi}^*}{\partial x_j} - \varepsilon_{ijk} f_j \overline{u_k} + \varepsilon_{i3k} f_3 \overline{u_{k_g}} + g\,\frac{\overline{\theta_v} - \theta_{v,ref}}{\theta_{v,ref}}\,\delta_{i3} - \frac{\partial \tau_{ki}^{r}}{\partial x_k} \tag{2}$$

$$\frac{\partial \overline{\theta_v}}{\partial t} = -\frac{\partial \overline{u_k}\bar{\theta}}{\partial x_k} - \frac{\partial H_k}{\partial x_k} + Q_\theta \tag{3}$$

$$\frac{\partial \bar{s}}{\partial t} = -\frac{\partial \overline{u_k}\bar{s}}{\partial x_k} - \frac{\partial W_k}{\partial x_k} + Q_w \tag{4}$$

In the above equations, the overbar indicates filtered quantities, and the indices $i, j, k \in \{1,2,3\}$ represent direction. ρ_0 (kg m^{-3}), $u_{k,g}$ (m s^{-1}), and f_i (s^{-1}) are, respectively, the dry air density, geostrophic wind, and Coriolis parameter. The symbols π^* and τ_{ki}^{r}, respectively, represent the modified perturbation pressure and deviatoric subgrid stress. $\overline{\theta_v}$ (K) and $\overline{\theta_{v,ref}}$ (K) are the virtual potential temperature and the virtual potential temperature of the reference state, while H_k and W_k, respectively, represent the subgrid scale (SGS) heat and scalar fluxes. Q_θ and Q_w indicate source/sink in the potential temperature and scalar equations, ε_{ijk} and δ_{i3} are the Levi-Civita symbol and Kronecker delta, g (m s^{-2}) is the acceleration due to gravity, and t (s) is time.

The SGS covariance terms in the PALM LES are parameterized following a 1.5-order closure scheme (Deardorff, 1980). The closure approach assumes that the SGS covariance terms are governed by eddy diffusivity, SGS turbulent kinetic energy, and local gradients of the mean flow variables. The SGS turbulent kinetic energy ($\bar{e}$) is determined by solving a prognostic equation (Eq. 5) that accounts for its production, dissipation, and transport within the subgrid scales.

$$\frac{\partial \bar{e}}{\partial t} = -\overline{u_k}\frac{\partial \bar{e}}{\partial x_k} - \tau_{ki}\frac{\partial \overline{u_i}}{\partial x_k} + \frac{g}{\theta_{v,ref}}\overline{u_3''\theta''} - \frac{\partial}{\partial x_k}\left(2k_m\frac{\partial \bar{e}}{\partial x_k}\right) - \epsilon \tag{5}$$

In this equation, τ_{ki} represents the subgrid stress tensor, $\overline{u_3''\theta''}$ denotes the SGS heat flux, k_m is the eddy diffusivity of SGS momentum, and ϵ represents the dissipation rate of $\bar{e}$ within a given grid volume.

Turbulence at the bottom boundary was treated by approximating surface momentum and heat fluxes using Monin-Obukhov similarity theory. This method assumes a constant flux layer between the wall and the first computational grid, allowing surface fluxes to serve as boundary conditions for the flow at the initial grid points (Maronga, 2014). The model uses a finite difference scheme for spatial discretization and a combination of a fifth-order upwind scheme (Wicker & Skamarock, 2002) and a third-order Runge-Kutta scheme for temporal discretization (Williamson, 1980), with timesteps satisfying the Courant–Friedrichs–Lewy condition of 0.9. Comprehensive explanations and formulations of PALM can be found in Maronga et al. (2015) and Maronga et al. (2020). In this study, PALM was modified to incorporate different local heat and scalar sources, enabling the use of a two-dimensional horizontal map of surface heat and scalar fluxes at the domain's bottom boundary, aligned with the grid resolution. The correctness of this modification and the model accuracy was tested afterward.

2.2. Model Validation

Various aspects of PALM have undergone extensive validation studies against field and laboratory-based experiments (e.g., Ardeshiri et al., 2020; Breton et al., 2017, 2017; Dey et al., 2023; Duan et al., 2019; Duan & Ngan, 2019; Gronemeier et al., 2021; Lo & Ngan, 2015; Lotrecchiano et al., 2020; Paleri et al., 2023; Park et al., 2012, 2013; Yaghoobian et al., 2014, to name a few) and widely applied to atmospheric flow problems. Here, we conducted two validation studies to assess PALM's performance in capturing the buoyant plume's characteristics, comparing results with the experimental measurements by Ezzamel et al. (2015) and Pham et al. (2005), and the LES result of Bhaganagar and Bhimireddy (2020).

Ezzamel et al. (2015) investigated buoyant turbulent plumes dynamics using particle image velocimetry. In their experiment, a plume was generated by introducing heated air, seeded with incense particles, through a turbulent grid into a neutral atmosphere. Temperature and velocity measurements were recorded at 0.01 m spatial intervals in both horizontal and vertical directions. The plume exhibited buoyancy of $g' = 0.0252$ cm s^{-2} and a Reynolds number of 1100 at the source. In their study, the plume buoyancy was defined as $g' = g\,\Delta T_0/T_0$, where g (m s^{-2}) is the acceleration due to gravity and ΔT_0 is the temperature difference between the heating element and ambient air temperature (T_0). Their experiments revealed the self-similarity of velocity profiles within the plumes and quantified the plume half-widths across different Richardson numbers.

For the validation study, the computational setup replicates the experimental setup of Ezzamel et al. (2015). Following Bhaganagar and Bhimireddy (2020), who compared their LES results against those of Ezzamel et al. (2015), a domain size of $10D$ (length) × $10D$ (width) × $17.5D$ (height), with D (= 400 m) being the diameter of the heat source, was used. The ambient atmosphere was neutral and quiescent, maintained at a constant potential temperature of 292 K (Ezzamel et al., 2015). The domain was discretized with a uniform horizontal grid size of 40 m and a vertical grid size of 10 m. Periodic boundary conditions were applied along the streamwise and lateral boundaries, while no-slip and free-slip boundary conditions were used, respectively, for the bottom and top boundaries. A circular heat source of a constant flux of 1 Km s^{-1} was located in the center of the bottom boundary.

To analyze the plume half-width and velocity distribution, time-averaged flow statistics over a 2000-second interval were computed after the plume fully developed. The plume edges were defined using a criterion of 0.5% of the time-averaged maximum buoyancy and 30% of the time-averaged maximum velocity along the centerline. From these edge locations, two plume half-widths were derived: one based on the buoyancy ($b_{g'}$) and the other based on the velocity magnitude ($b_{w'}$), plotted in Fig. 1a. As can be seen in this figure, the predicted plume half-widths using both criteria compare well with the experimental results of Ezzamel et al. (2015).

Additionally, the time-averaged non-dimensional vertical velocity profiles ($\overline{w}/\overline{w_c}$) were analyzed along the radial direction (x/D) at four vertical heights $z/D = 1.8$, 3.2, 6.0, and 8.8. These values were compared against the experimental data in Fig. 1b. The velocity values were made non-dimensional using the mean vertical centerline velocity ($\overline{w_c}$) at the corresponding vertical heights. As observed in the experiments, the profiles exhibit self-similarity and collapse over one another. Overall, PALM's results demonstrate strong agreements with the experimental results.

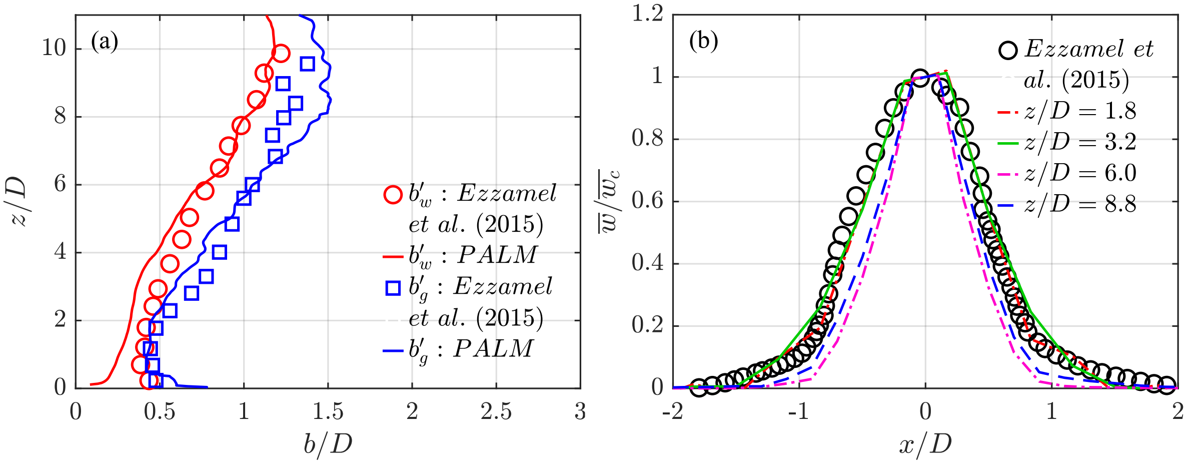

Fig. 1: Comparison of PALM's computational results and experimental data of Ezzamel et al. (2015) for (a) vertical profiles of plume half-width and (b) non-dimensional radial variations of plume vertical velocity at different vertical locations within $1.8 < z/D < 8.8$. In (b), the symbols show the experimental results for $z/D = 1.8$. The experimental plots for the other heights (not shown) nearly overlap this curve.

A second validation study was performed in which we compared PALM's results against experimental data of Pham et al. (2005). Pham et al. (2005) investigated pure thermal plumes under similar ambient conditions using particle image velocimetry. Their experimental setup had a metallic heating source with a diameter of 0.1 m and a thickness of 0.02 m, positioned in an enclosure measuring 2 m (length) × 2 m (width) × 2.5 m (height). The heating source was mounted 0.01 m above the enclosure floor, and the ambient environment was maintained at a constant temperature of 292 K. Pham et al. (2005) reported that the mean centerline velocity decayed with an exponent of -1/3 after reaching its peak value, while the mean temperature difference between the plume and the surrounding atmosphere exhibited a decay rate of -5/3. Bhaganagar and Bhimireddy (2020) reported similar decay trends in their numerical results.

Figure 2a and 2b illustrate the variations of the normalized mean centerline velocity ($\overline{v}_c/(\overline{v}_c)_{max}$) and normalized mean difference between the centerline and ambient temperatures ($\overline{\Delta\theta}/(\overline{\Delta\theta})_{max}$) with height ($z/D$). For both plots, the maximum value of the centerline velocity and temperature difference were used as the normalization parameter. Figure 2 also includes the LES results of Bhaganagar and Bhimireddy (2020). The results indicate a strong agreement between PALM's predictions and the experimental observations from Pham et al. (2005).

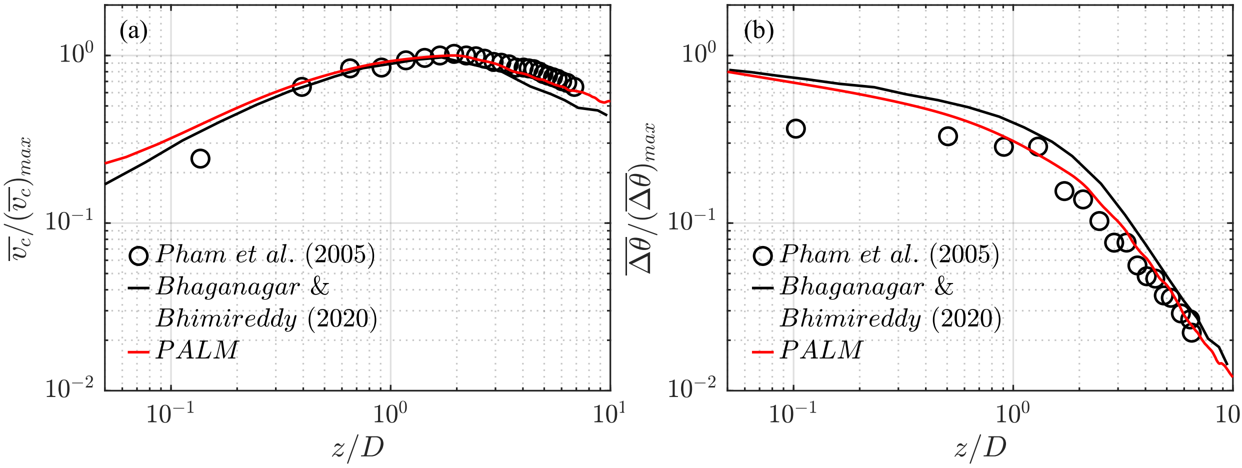

Fig. 2: Comparison of vertical profiles of (a) normalized mean centerline velocity and (b) normalized mean difference between the centerline and ambient temperatures.

2.3. Simulation Setup

To investigate plume dynamics and dispersion behavior under various atmospheric stability conditions, we first initialized the simulation domains (Fig. 3) with turbulent flows of three distinct atmospheric stability states: neutral, unstable, and stable. This was done using a mean wind velocity of 5 m s^{-1} entering a cubical domain from the left, and by maintaining the surface temperature above (by 5 K) and below (by 10 K) the air temperature for the unstable and stable cases, respectively. To accelerate simulation convergence and to precondition the domain, each case was initialized by imposing initial mean vertical profiles of potential temperature representative of typical daytime (unstable), nighttime (stable), and neutral stability conditions (based on Table 1). Following this and after the turbulent boundary layer flow fully developed and the flow reached a quasi-steady state for each case, we introduced the plume into the domain by imposing a circular heat and scalar source. The source was implemented at the first grid above the bottom boundary to be consistent with the treatment of the near-surface turbulence by the Monin-Obukhov similarity theory. The source, with a diameter (D) of 500 m, was positioned at a distance of 10 km from the domain inlet and equidistant from the lateral boundaries. The heat and scalar fluxes from the source were, respectively, set to 129.94 kW m^{-2} (= 100 K m s^{-1}) and 100 kg m^{-2} s^{-1}.

Table 1: Initialization parameters for the different atmospheric stability conditions. $z_{i,0}$ is the prescribed height of temperature inversion.

Stratification	**Surface temperature (K)**	**Temperature gradient (K/100 m)**	$z_{i,0}$ **(km)**
Neutral	300	0	$z_{i,0} > 0$
Unstable	305	-0.3 0 0.1	$0 < z_{i,0} < 0.5$ $0.5 < z_{i,0} < 3$ $z_{i,0} > 3$
Stable	290	0.3 0	$0 < z_{i,0} < 3$ $z_{i,0} > 3$

Large computational domains were considered for the simulations, measuring 48 km in length and 20.4 km in width providing domains over at least 30 times the integral length scales of the most energetic eddies in the domain (Fig. 3). Given the nature of plume development (which will be discussed later) a large enough domain height is required. To choose an appropriate domain height, several tests were conducted to ensure that the domain top boundary has minimum (in case of the neutral stability) to no effect (in the unstable and stable cases) on the plume development. Therefore, domain heights of 16.1 km, 12.42 km, and 8.28 km were, respectively, chosen for the neutral, unstable, and stable cases. The lateral boundaries were treated as periodic, however, the large length of the domain allowed for the plume to reach a quasi-stationary state way before the plume crossed the domain boundary. At the bottom boundary, a no-slip condition with a surface roughness of 0.05 m was applied, while the top boundary was set to zero-gradient Neumann condition. To prevent the reflection of gravity waves downwards, flow damping was implemented at the heights of 13 km, 8 km, and 4.8 km for the neutral, unstable, and stable conditions, respectively. Due to the nature of the problem, the Coriolis forces were not considered in the simulations.

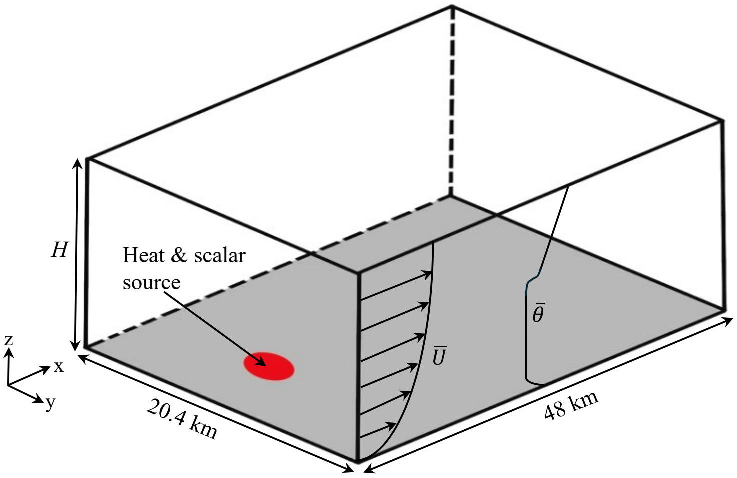

Fig. 3: Computational domain employed for the current study, with representative temperature and velocity profiles varying across different cases. The domain height (*H*) was variable between cases, being 16.1 km, 12.42 km, and 8.28 km for the neutral, unstable, and stable cases, respectively. The source diameter is 500 m and is located 10 km from the domain inlet. The dimensions are not to scale.

Given that the atmospheric boundary layer flows exhibit varying characteristics across different length scales depending on the atmospheric stratification, well-resolved simulations of these flows necessitate distinct grid sizes (Wurps et al., 2020). Consequently, a grid sensitivity analysis was conducted to determine the optimal grid size for each stability case, taking computational expenses into account. For the grid sensitivity analysis, simulations were performed using grid spacings of 75 m, 50 m, and 40 m for each scenario, while an additional case with a grid size of 25 m was tested for the stable condition. Through evaluating the mean profiles of several parameters, including the streamwise velocity, potential temperature, friction velocity, turbulent kinetic energy (TKE), and resolution ratio (defined as the ratio of resolved and total TKE), together with eddy integral length scale resolution, it was indicated that a grid resolution of 50 m is adequate to represent the flow characteristics in the neutral and unstable cases, while a grid spacing of 25 m is fine enough to correctly capture the flow physics in the stable scenario (more information regarding the grid independency analysis is provided in Appendix A).

Grid stretching was implemented for manageable and efficient computations. To determine the grid topography and stretching height within the domain, the approximate plume rise height was estimated for the stable and unstable cases using several preliminary simulations (it should be noted that the plume behavior and rise height are different under different atmospheric conditions, which will be discussed in detail later). Uniform horizontal and vertical grid spacing was maintained up to above the plume rise heights (i.e., 6.6 km (unstable) and 4.2 km (stable)), beyond which the grids were stretched vertically by a factor of 1.08. In the neutral case, given the continuously rising nature of the plume, a uniform grid topography would be ideal. However, due to the computational expenses, the grids were maintained uniform up to 12 km, and then vertically stretched by a factor of 1.08.

3. Results and Discussions

3.1. Background atmospheric conditions

As mentioned earlier, the simulations were initialized with the typical daytime (unstable), nighttime (stable), and neutral atmospheric turbulent flow conditions before the introduction of the plume. Each simulation progressed for a minimum spin-up time of 25 large eddy turnover times to reach a quasi-steady state, followed by time averaging over the last 7200 s (equivalent to over 2 large eddy turnover times in the domain). For the unstable case, the large eddy turnover time was calculated as the ratio of the boundary layer height (equivalent to the inversion height) and convective velocity (Raasch & Etling, 1991; Wurps et al., 2020), while for the neutral and stable conditions, it was defined as the ratio of the boundary layer height to friction velocity (Moeng & Sullivan, 1994; Wurps et al., 2020). The stable and neutral boundary layer heights were defined as the height at which the vertical momentum flux ($u'w'$) reaches 5% of its value at the surface.

Figures 4a and 4b, respectively, show the temporally and horizontally averaged vertical profiles of the streamwise velocities and potential temperatures for the three cases. Under the neutral condition, where there is no significant temperature gradient affecting buoyancy, a well-mixed boundary layer forms due to the shear forces. Near the surface, up to about 4 km in our case, the mean velocity follows a typical logarithmic profile, while above this layer, the velocity gradient decreases, resulting in a nearly linear profile with height, ultimately matching the inflow velocity. The potential temperature is constant (at 300 K) with height throughout the boundary layer.

During the daytime, solar heating raises the surface temperature above that of the surrounding air, creating an unstable boundary layer with strong buoyancy. Like the neutral condition, near the surface (up to ~0.3 km), the mean velocity follows a logarithmic profile, while due to buoyant turbulence, a convective mixed layer forms until ~4 km, leading to a reduced wind speed and relatively constant velocity and temperature profiles with height. Above this region, the inversion layer acts as a cap, inhibiting vertical motions and compressing the turbulent eddies below it. This compression leads to the accumulation of momentum and a localized increase in the streamwise velocity at about 4.6 km height.

At night, the surface cools rapidly through radiative cooling, resulting in a stable boundary layer where the surface temperature is lower than the air temperature above. Within this layer, the wind increases almost linearly with height, while due to negative buoyancy, the flow experiences reduced turbulence and vertical mixing. The stable boundary layer is topped with a slightly increased wind speed aloft, commonly referred to as the low-level jet. The resulting potential temperature profile, after the simulation reached a quasi-steady state, reflects a blend of the well-mixed and linearly-mixed idealized nighttime potential temperature profiles (Stull, 2012), exhibiting a shallow boundary layer height of ~600 m.

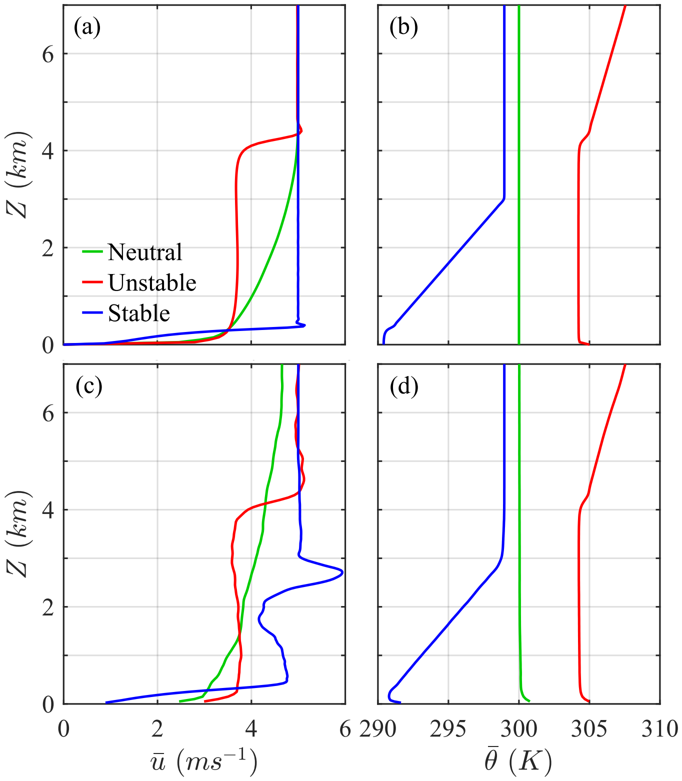

Fig. 4: Temporally and horizontally averaged vertical profiles of streamwise velocity (left panel) and potential temperature (right panel) before (a and b) and after (c and d) the initiation of the heat and scalar fluxes. The figures display the profiles up to a height of 7 km, beyond which the profiles maintain their trends to the top of the domain in each case.

3.2. Plume initiation and development, and its effect on the background flow

After the introduction of the heat and scalar sources into the domain, the plumes start developing and evolving into the fully developed atmospheric boundary layers. The introduction of a heat source can potentially modify the local prevailing atmospheric conditions, depending on the temperature gradient created by the source. We reexamined the time and horizontally averaged vertical profiles of the streamwise velocities and potential temperatures of the background flow after the introduction of the plume (Fig. 4c, 4d). The profiles are spatially and time-averaged over the last 1800 s of the plume transport. The rationale for selecting this averaging period is discussed in the following section (Sect. 3.3). The locations where spatial averaging was performed have fully developed plumes in a quasi-steady state.

In all cases, the introduction of the plume caused a decrease in the mean streamwise velocity up to the maximum plume rise height. This decrease is small in the unstable case because the enhanced mixing (in the mixed layer) rapidly distributes the plume’s momentum and heat, minimizing the velocity deficit. However, the wind velocity reduction is notable in the neutral and stable cases. It can also be noted that at the maximum plume rise height, the streamwise velocity increases in the stratified cases. Under the unstable case, this increase is minor, however, in the stable case, this increase is significant as the stable stratification limits vertical mixing, leading to a more pronounced horizontal acceleration of the flow. The effect of the plumes on the local atmospheric potential temperature profile was small and mainly limited to the region close to the ground surface as can be seen in Fig. 4d.

The mid-span vertical cross-sections of the instantaneous (Fig. 5) and mean (Fig. 6) normalized scalar density contours reveal that the shape and development characteristics of the plumes vary significantly under different stability conditions. Before going into the details, it should be noted that since this study focuses on phenomena occurring in the atmospheric boundary layer, where variations align with atmospheric scales, it is logical and intuitive to report distances in dimensional forms, such as kilometers. However, for greater generality, we present the streamwise distances in Fig.

5 also in a non-dimensional form, using the plume source diameter as a normalization parameter.

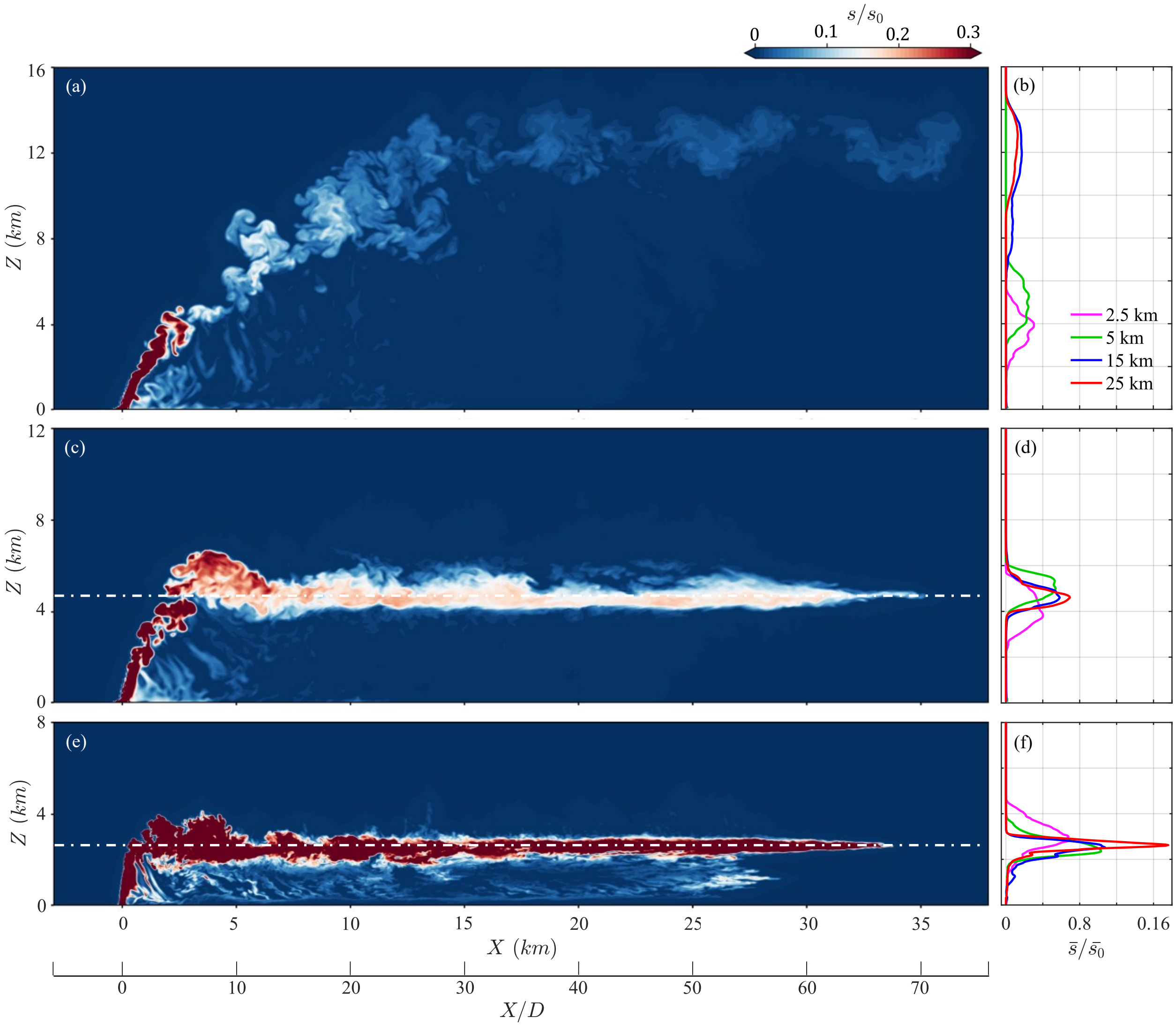

Fig. 5: Vertical cross-sections of the instantaneous normalized scalar density contours at the middle of the domain (left panel) and time and spanwise plane-averaged normalized scalar density plots (right panel) under different stratification conditions: (a, b) neutral, (c, d) unstable, and (e, f) stable. The plume snapshots were obtained at $55D/U_\infty$ (s) after the heat and scalar fluxes were initiated, with D and U_∞, respectively, being the source diameter and freestream velocity. The dotted white line indicates the approximate height of the inversion layer.

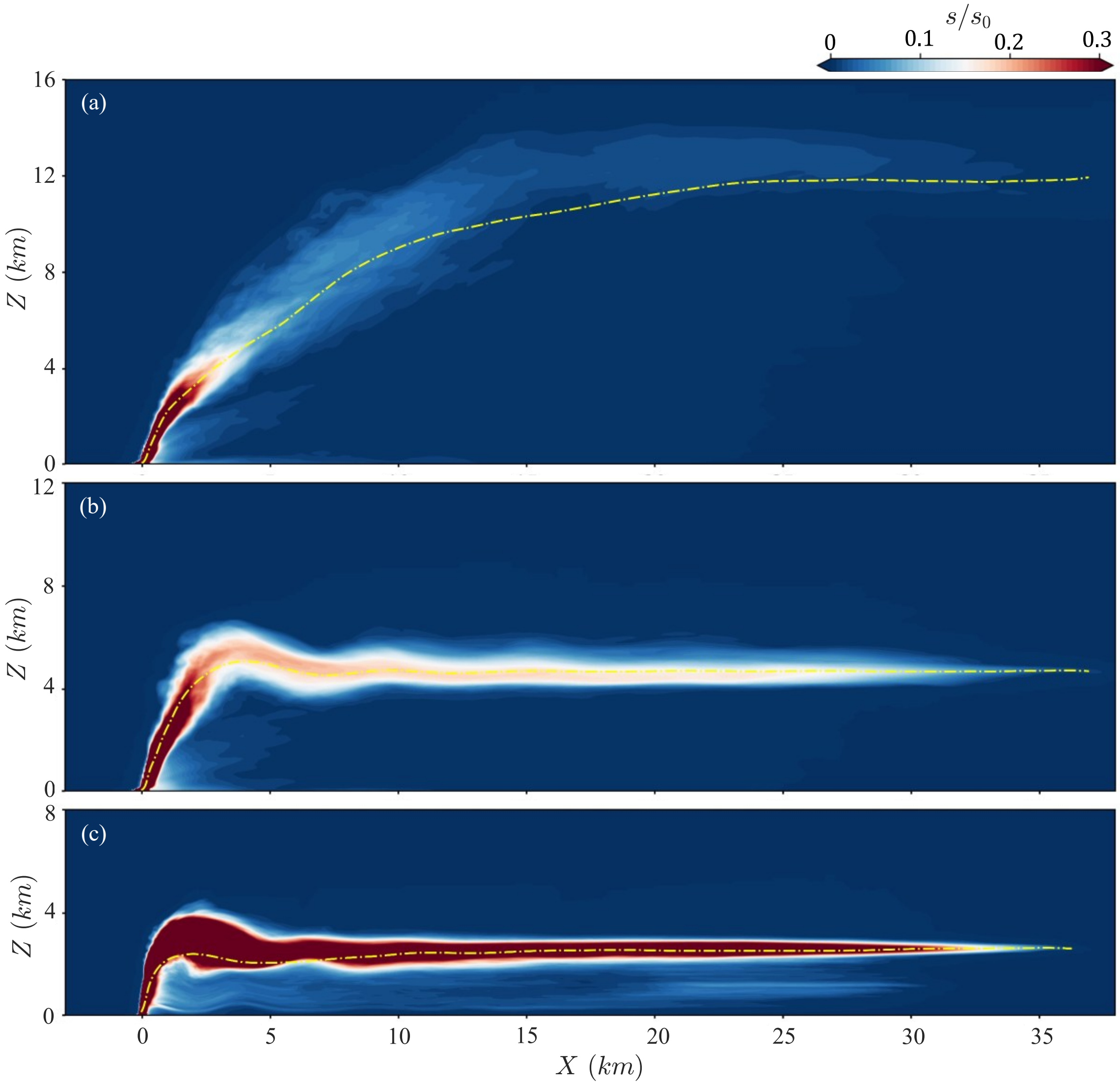

Fig. 6: Vertical cross-sections of the time-averaged normalized scalar density contours at the middle of the domain under different stratification conditions: (a) neutral, (b) unstable, and (c) stable. The dotted yellow line indicates the time averaged plume centerline, with details on its calculation provided in Sect. 3.3. Both the plume and centerline are averaged over a duration of 1800 s.

The average plume rise height varies between cases and is constrained by the inversion layer height under the non-neutral conditions, reaching about 4.6 km and 2.6 km in the unstable and stable cases, respectively. In these cases, the plume slightly overshoots and penetrates the inversion layer before traveling downstream with the wind, forming a small bulge. Under neutral conditions, the plume height primarily depends on the source buoyancy flux and ambient wind speed, but under the current simulation setup, it is limited by the domain height as it continues growing. From the scalar density contours (Fig. 5 and Fig. 6), it can also be noted that under different stability conditions, the plume makes different angles with the ground surface as it grows vertically. This angle depends on the balance between the plume's buoyant force and the shear force from the crossflow. In the neutral scenario, where the background flow lacks buoyancy to either support or oppose the plume's vertical motion, the plume has the greatest inclination, forming an angle of 63° with the surface at the steady state. Under the unstable condition, where buoyancy in the background convective mixed layer aids vertical air movements, the plume stands more upright at 70°. Under stable stratification, due to the high-temperature gradient between the plume and the surrounding air and the significant buoyant forces, the plume is most upright, reaching an angle of 81°. To help with the discussion, a figure of the vertical cross-sections of the normalized mean potential temperature contours for all cases is included in Appendix B, providing visuals of mean temperature differences between the plume and background flow. The results also indicate that due to the different stability conditions, the scalar density within the developing plume is significantly different between the three cases. The right-side panel in Fig. 5, shows the time and yz-plane-averaged scalar density ($\bar{s}$), normalized by the scalar density at the source ($\bar{s_0}$), at several downstream locations. $\bar{s_0}$ was obtained using the scalar flux (100 kg $m^{-2}s^{-1}$) and the buoyant velocity of the plume, w_p, defined by Eq. 6 (Bhaganagar & Bhimireddy, 2020).

$$w_p = \sqrt{gD\frac{\Delta\rho}{\rho_0}} \tag{6}$$

Here, g (m s^{-2}) is the acceleration due to gravity, and $\Delta\rho$ (kg m^{-3}) is the density difference between the plume and the ambient air (ρ_0) at the source. It can be seen that the highest scalar density was observed under the stable scenario (Fig. 5e, 5f, and Fig. 6c).

Although the vertical scalar distribution (along the *z*-axis) remains Gaussian with its peak centered slightly below the inversion layer, a secondary small peak is observed in this case at 15 km and 25 km downstream of the heat source (Fig. 5f). The secondary peak results from the scalars being carried downstream by the low-level jets. The wind shear associated with the low-level jets facilitates the long-range transport of scalars below the inversion layer and promotes vertical momentum transport toward the surface (Blackadar, 1957; Mahrt, 1998; Wei et al., 2023). In the unstable case, the scalar density is lower than that in the stable case and follows a Gaussian distribution centered close to the inversion layer (Fig. 5d). Unlike the stable scenario, in which the scalar density increases as the plume travels downstream, the maximum scalar density in the unstable situation remains within the same range. Under the neutral condition, the scalar density is lower than the other two cases and decreases as the plume progresses downstream. Unlike the stratified cases, the Gaussian plume distribution in the neutral situation has a wide profile, indicating significantly greater vertical dispersion (Fig. 5b).

Another phenomenon that can be observed in the dynamics of these plumes developing in a crossflow is the presence of streak-like structures extending from the underside of the plume to the ground. These structures, previously identified as wake vortices, are upright vortices that form downstream of jets (Fric & Roshko, 1994; Mahesh, 2013) and buoyant plumes (Finney et al., 2021). These vortices play an important role in transporting passive scalars from the primary jet envelope toward the wall boundary, thereby enhancing the scalar mixing process (Uyanwaththa et al., 2019). In the neutral case, the wake vortices are more coherent and extend downstream, sometimes up to 5 km from the source, thereby enhancing the vertical scalar dispersion. In the stable and unstable cases, these vortices are observed closer to the heat source at distances of about 1 – 2 km. Far from the source, in the unstable case, the wake vortices quickly dissipate and become more fragmented due to enhanced mixing, while in the stable case, these vortices do not persist over long distances due to their interaction with the low-level jets.

A notable difference between these plumes, not apparent in Fig. 5 and 6, is the speed at which the plume propagates. Understanding the propagation speed is important in determining how quickly the plume spreads downstream. To access this, we extracted the rate of spread (ROS), which represents the velocity of the plume's leading edge in the streamwise direction. The ROS was computed by tracking the time-varying iso-contour of the scalar density at 0.01 kg m^{-3}. By monitoring the plume's farthest extent in the streamwise direction over time, we determined the ROS based on the time required for the plume to traverse a 1 km segment. Figure 7 plots the ROS (m s^{-1}), normalized by the freestream velocity, U_∞, along the streamwise direction. Close to the heat source, the plume's ROS is the highest in the unstable case. In both stratified cases, the plume initially penetrates the inversion layer before experiencing deceleration, resulting in a noticeable decrease in the rate of spread at approximately 3 km and 6 km for the stable and unstable scenarios, respectively. As the plume continues downstream, the normalized ROS stabilizes at nearly constant values of 1.17 for the stable and 1.2 for the unstable cases. The ROS in the neutral case exhibits persistent fluctuations around a mean value of 1.34 until the plume reaches the top region of the domain approximately 15 km downstream from the source. Beyond this point, the results of the neutral case are influenced by the top boundary and the courser grid resolution beyond the 12 km height.

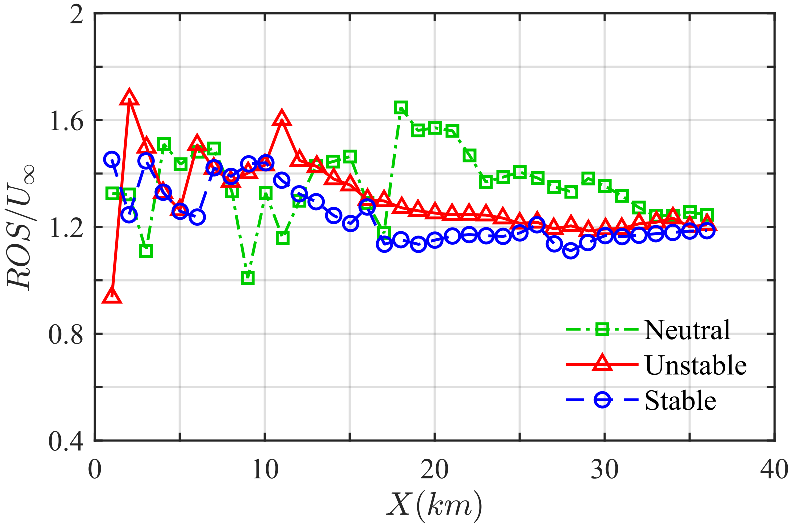

Fig. 7: Normalized plume rate of spread (ROS) in the streamwise direction downstream of the source. $U_\infty$is the freestream velocity.

3.3. Mean flow characteristics of the plume

To investigate the underlying mechanisms of plume dynamics under the effects of atmospheric stratifications, we first focus on the mean flow behavior along the plume centerline. The plume centerline can be determined using various methods (Jordan et al., 2022), including identifying the locations of maximum velocity magnitude, maximum buoyancy, maximum TKE, or the center of mass of scalar density, buoyancy, or velocity magnitude. In this study, after examining different methods, we chose to determine the plume centerline by calculating the center of mass of the scalar of the time-averaged plume (Fig. 6). To determine the center of mass for each streamwise (x) location, we computed the spanwise (Y_c) and vertical (Z_c) coordinates using the following method: the spanwise (Y_c) coordinate was obtained by taking the ratio of the $\sum y \times s(y,z)$ to $\sum s(y,z)$ over the yz-plane, while the vertical (Z_c) coordinate was determined by calculating the ratio of $\sum z \times s(y,z)$ to $\sum s(y,z)$ over the yz-plane. Here y and z represent the spanwise and vertical locations, respectively, and $s(y,z)$ denotes the scalar density.

To determine the optimal averaging duration, we tested three time intervals: 600 s, 1200 s, and 1800 s, after the plume reached a quasi-steady state. By examining the magnitude of velocity components and temperature along the plume centerline for each interval, we observed small differences and statistical convergence between the two longer periods. Therefore, the 1800 s interval (equivalent to over $100t_p$, with $t_p = D/w_p$ being the plume time scale) was selected for our analysis. For consistency, all centerline plots are presented up to 25 km, where data is available over the entire 1800 s.

Figure 8 shows the normalized mean velocity magnitude along the plume centerline, with Fig. 8a using buoyancy velocity (w_p) and Fig. 8b using background bulk wind velocity (u_b) as the normalization parameter. It should be noted that due to different background atmospheric stratifications, w_p varies across the three cases, indicating 31.34 m s^{-1} for the neutral, 31.54 m s^{-1} for the unstable, and 38.68 m s^{-1} for the stable cases. For the stratified scenarios, u_b was calculated as the average velocity below the inversion layer, whereas for the neutral case, it was calculated as the average velocity over the entire domain height, resulting in bulk velocities of 4.79 m s^{-1}, 3.81 m s^{-1}, and 4.66 m s^{-1} for the neutral, unstable, and stable cases, respectively.

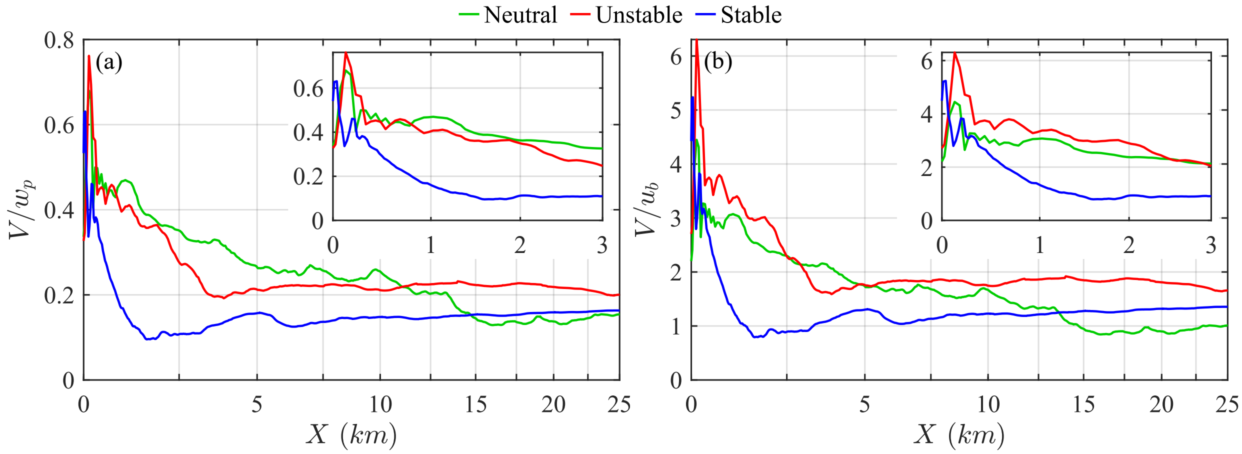

Fig. 8: Variation of the temporally averaged velocity magnitudes along the plume centerline (a) normalized by the plume buoyancy velocity, and (b) normalized by the background bulk velocity.

Near the heat source, the plume reaches a maximum mean velocity magnitude for all cases. It can be noticed that close to the heat source (within the first 0.7 km) the V/w_p profiles for the neutral and unstable cases nearly collapse. This suggests that in this region, the plumes in these scenarios follow similar scaling laws and are dominated by similar physical mechanisms governed by the buoyancy of the heat source. The lack of such behavior in the same region in Fig. 8b adds that the dynamics of the plumes near the source are not much influenced by the background wind. Under the stable condition, the maximum mean V/w_p is lower due to the stable boundary layer suppressing the plume vertical movement. These results indicate that, for the conditions considered in this study, near the source, atmospheric conditions have a weak effect on the plume mean centerline velocity in the unstable case but a significant effect in the stable scenario.

The subsequent deceleration in the centerline mean velocity magnitude is more rapid in the stable case as the plume reaches the inversion height earlier (~1 km from the source). In Fig. 8b, we observe that near the source, the plume in the unstable case attains the highest mean velocity magnitude with respect to the background velocity (6 times), followed by that of the stable case. While, near the heat source, the plume dynamics are mainly influenced by the plume buoyancy, farther from the source, in regions where the neutral plume is not yet affected by the domain's upper boundary, a relatively close behavior can be seen between the scaled velocity profiles of the neutral and unstable cases. We speculate that if the plume in the neutral case were unaffected by the domain top boundary, its normalized velocity profile in Fig. 8b would follow that of the unstable case. This behavior, along with the increasing trend of the normalized velocity profile of the stable case, suggests that if the domain was much longer in the streamwise direction, the three profiles in Fig. 8b would eventually converge to an asymptotic value of 1, with plume dynamics fully controlled by the background flow conditions.

Figure 9 shows the normalized mean velocity components along the plume centerline. Near the heat source, vertical velocity (Fig. 9c) increases across all cases, as expected from the buoyant plume rise. The unstable case exhibits the largest increase, driven by the combined effects of the heat source and background buoyancy. As the heated plume rises, it entrains ambient air horizontally into the plume. Near the heat source, this entrainment generates opposing streamwise velocities: negative on the right side and positive on the left side of the plume. At the point where the velocity magnitude within the plume's cross section is highest, these opposing horizontal velocities are expected to cancel each other out. However, since the plume centerline is calculated based on the scalar's center of mass—and the scalar density is not uniform across the cross-sections (as discussed later; Fig. 10)—the centerline may deviate from the location of maximum velocity. The negative streamwise velocity observed near the heat source in Fig. 9a indicates entrainment of ambient air from the plume's right side, where the centerline sampled the flow. Among the cases, entrainment of the streamwise velocity in the stable case is slightly larger than the other cases due to the higher temperature gradient between the plume and the ambient air in this case.

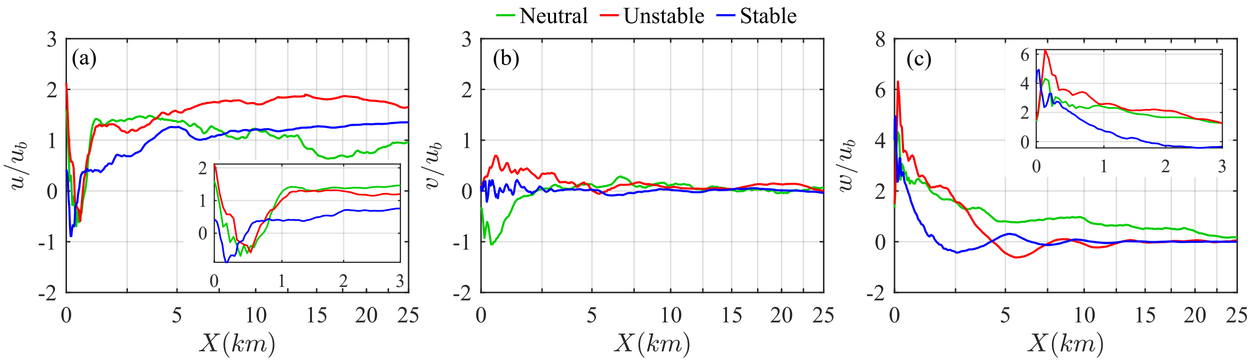

Fig. 9: Variation of the temporally averaged and normalized (a) streamwise, (b) spanwise, and (c) vertical velocities along the plume centerline.

The centerline spanwise velocity (Fig. 9b) has small magnitudes compared to the other velocity components. However, close to the heat source, it is non-zero for the unstable and neutral cases, indicating greater instabilities and spanwise oscillations of the plume around the centerline compared to the stable case. This behavior is also visible in the mean scalar contours of the plume in the *yz*-plane near the source (not shown). Farther from the heat source, the mean spanwise velocity decreases to small magnitudes across all cases with only minor oscillations.

As expected, the vertical velocity is the dominant velocity component near the buoyancy source, increasing significantly before gradually decaying downstream (Fig. 9c). While near the source the maximum mean vertical velocity is the largest for the unstable case, its decay is most rapid in the stable boundary layer. In both the stratified cases, shortly after the plume reaches the inversion height, its vertical velocity is halted and oscillates around zero. The oscillation is due to the entrainment of the warmer air from above this height. Although these oscillations reduce in magnitude downstream, they remain non-zero throughout. In contrast, the neutral plume, unrestricted by an inversion layer, maintains a higher mean vertical velocity than the stratified cases as it travels away from the source.

Entrainment of the momentum and ambient cooler air into the buoyant jet is an important characteristic that is responsible for the jet plume mixing and cooling and its radial growth. An important question is how the stability condition of the atmospheric boundary layer affects the plume radial expansion as it indicates the diurnal impact of plumes on downstream regions. Figure 10 presents *yz*-cross sections of the plumes under the three different stability conditions, 12 km downstream of the source. These sections utilize the normalized mean scalar density field and are overlaid with the normalized mean velocity vectors at the same cross-section. The general difference in the shape of the plume cross-sections persists relatively the same between the three cases after the plume hits the inversion height in the stratified cases. We can see that the plume in the neutral case develops counter-rotating vortex pairs, a phenomenon that is absent in stratified cases. The formation of these vortex pairs, well documented in previous studies of jets and plumes (Church et al., 1980; Cortelezzi & Karagozian, 2001; Finney et al., 2021), is attributed to the interaction between the vertical vorticity (horizontal vortices) in the crossflow and the plume (Cunningham et al., 2005). The crossflow's horizontal vortices tilt upward within the plume, creating two vortex pairs rotating in opposite directions along the plume's flanks. Although not shown here, as the plume progresses downstream in the neutral case, these vortex pairs tend to drift apart, with the highest scalar densities concentrated within the vortex cores. The vortex formation induces positive vertical velocity along the plume centerline and high-velocity magnitudes within the vortex pairs.

In the unstable case, strong vertical convection (and high mixing) in the background tends to disrupt and break up the horizontal shear layer structures, that would otherwise interact with the plume to form vortex pairs. Conversely, in the stable case the strong stratification, and inhibited vertical motion, prevents the tilting and rolling of horizontal vortices in the vertical direction, thereby inhibiting the formation of counter-rotating pairs. Both the unstable and stable cases show lower velocity magnitudes within the plume. In addition, in the unstable case, convective cells in the ambient background enhance air entrainment, causing the plume to meander slightly off-center due to the pulsating nature of these cells. The stable case with minimal entrainment and dispersion, maintains a relatively symmetrical plume with the highest scalar density concentrated in the core. The neutral case also exhibits a symmetrical plume due to limited mixing and the absence of coherent structures in the background flow.

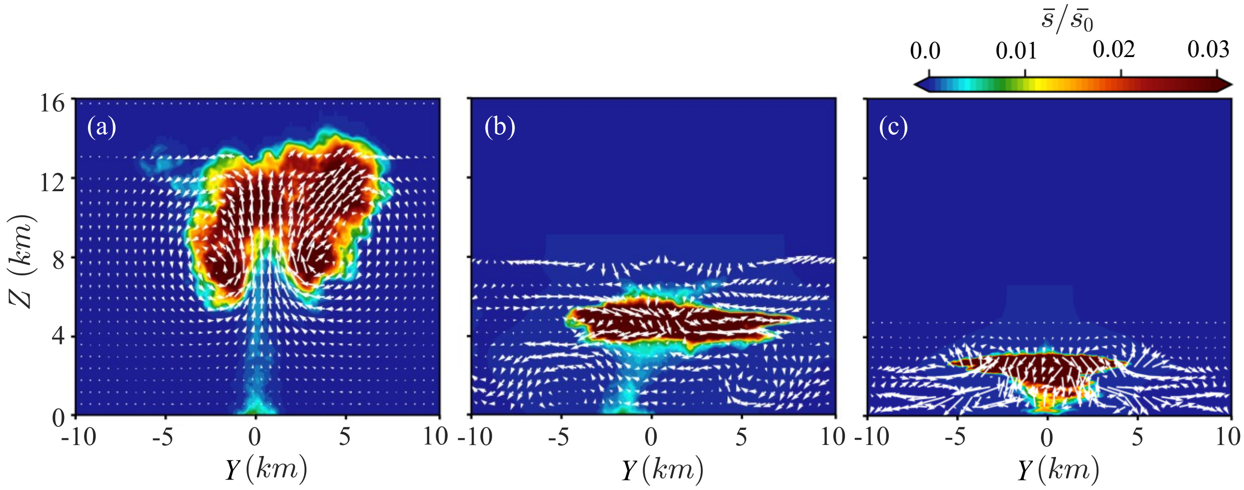

Fig. 10: Spanwise cross-sections of the temporally averaged normalized scalar density contours at 12 km downstream of the heat source under (a) neutral, (b) unstable, and (c) stable stability conditions. The vectors show the normalized mean velocity vectors, scaled by the bulk velocity, u_b.

It can also be seen that the plume's radial extent about the centerline in Fig. 10 varies with atmospheric stability. The neutral atmosphere allows the plume to spread the widest, while the stable atmosphere limits the radial expansion. Figures 11a and 11b, respectively, show the changes in the spanwise and vertical growth of the plume along the plume centerline, based on the spanwise and vertical standard deviations of the plume size.

In all the stability cases, after the initial formation of the plume neck near the source, the plume's width increases steadily downstream (Fig. 11a). However, the growth pattern varies based on the atmospheric conditions. For instance, in the unstable case, due to vigorous vertical mixing driven by convective activity, the plume width continues to increase until approximately 13 km downstream, where it levels off, reaching a maximum width of 20 times the source diameter. In the stable case, where background turbulence is weaker and vertical mixing is suppressed, the plume reaches a maximum width of 16 times the source diameter, but only after 17 km downstream. The reduced turbulence in the stable atmosphere inhibits mixing, constraining the plume's lateral spread. In contrast, the unstable atmosphere, with its stronger turbulence, encourages more mixing, allowing the plume to spread wider throughout its downstream progression. This difference in mixing intensity is a key factor that leads to the consistently larger plume width in the unstable case.

Similarly, the plume's vertical expansion behaves differently in each stability scenario. In the neutral case, the plume height grows consistently with the downstream progression until it reaches the top of the domain, where it is limited by the simulation boundary. In the stratified cases, the plume's vertical growth is initially rapid, with the unstable case expanding vertically within the first 2 km and the stable case within 4 km. However, both cases encounter the inversion layer, where the plume attains a maximum height of 8 times the source diameter in the unstable case and 5.5 times the source diameter in the stable case. Beyond 23 km from the source, the radial size of the plume begins to decrease in both the unstable and stable cases, marking the formation of the plume tip, as also seen in Fig. 5 (left panel). This tip formation results from the interaction between the plume and the background stratification, which confines the plume's vertical and lateral expansion. This behavior is absent in the neutral case. The variations in the plume radial expansion along the plume centerline result in changes in the plume scalar density, as seen in the right panel of Fig. 5.

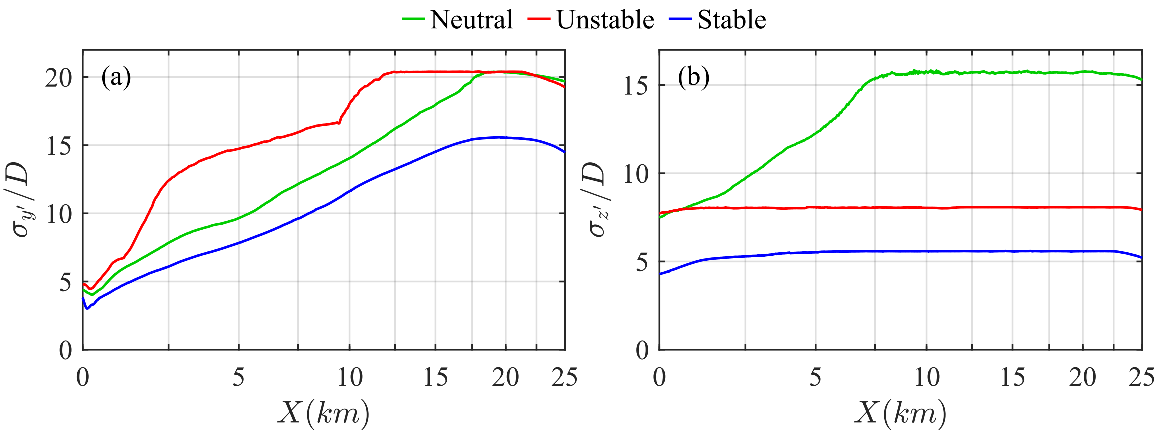

Fig. 11: Time-averaged variation of the plume local (a) width and (b) height along the plume centerline.

3.4. Energy distribution within the turbulent plume

To assess the turbulence intensity within the plume, the TKE along the plume centerline was analyzed under the three stability conditions (Fig. 12). In all cases, TKE $\left(0.5\left(\overline{u'^2}+\overline{v'^2}+\overline{w'^2}\right)\right)$ peaks near the heat source and then gradually diminishes. The stable scenario exhibits the highest and earliest TKE peak, driven by the pronounced temperature gradients between the plume and the surrounding flow. Farther from the source, where TKE consistently decreases, the neutral case maintains the highest TKE levels, while the stable scenario shows the lowest. TKE is closely related to the mixing and transport processes within the flow, with higher TKE regions promoting enhanced mixing and dispersion of momentum, heat, and scalar quantities. This explains the observed plume density variations, with the neutral case showing the lowest plume density and the stable case the highest, as depicted in Fig. 5.

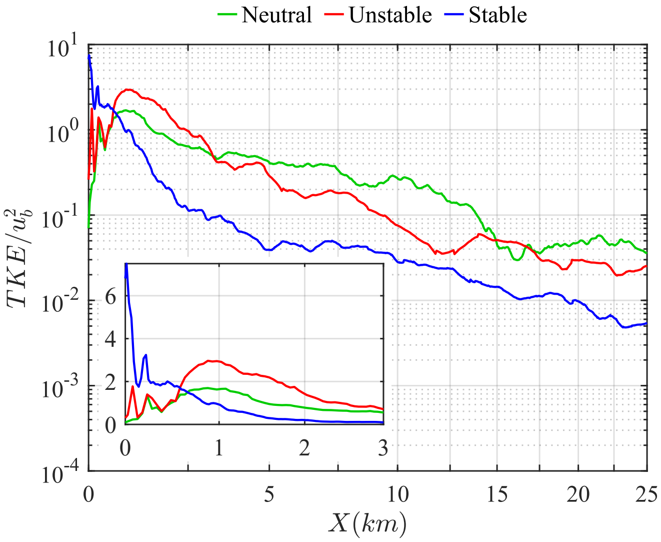

Fig. 12: Variation of the temporally averaged normalized turbulent kinetic energy (TKE) along the plume centerline.

While TKE quantifies the energy within the turbulent plume and measures the intensity of velocity fluctuations, understanding how vortices transport this energy within the plume is fundamental. Turbulent flows are inherently characterized by rotational motions, quantified by vorticity (ω). A key mechanism responsible for the dispersion of turbulent velocity fluctuations, or flow energy, is the transfer of vortical energy. This vortical energy, or enstrophy ($\varepsilon = \overline{\omega_x'\omega_x'} + \overline{\omega_y'\omega_y'} + \overline{\omega_z'\omega_z'}$), is important for understanding the processes of dissipation, mixing, and the complex dynamics of plumes. Figure 13 compares the time and spatially averaged streamwise ($\overline{\omega_x'\omega_x'}$), spanwise ($\overline{\omega_y'\omega_y'}$), and vertical ($\overline{\omega_z'\omega_z'}$) enstrophy components along the horizontal direction for the three stability cases, each normalized by their maximum values. To estimate the enstrophy components along the plume development direction, spatial averaging was conducted across each yz-plane in the horizontal direction. This allows us to capture the intensity of rotational motions across the entire span of the plume, rather than focusing solely on the centerline. In all cases, the vorticity variances rise from the source and reach their maximum values before starting to decay. Regardless of the stability condition in the background flow, the components of enstrophy reach their peak very close to the heat source ($< 1D$ for the streamwise and spanwise components and $< 1.6D$ for the vertical component). The variations in the peak location of the horizontal and vertical components of enstrophy are due to the different mechanisms these vortical energies represent. Streamwise and spanwise enstrophy are primarily influenced by the gradients in the vertical velocity fluctuations ($\partial w'/\partial x, \partial w'/\partial y$). Because vertical velocity is the highest near the heat source, horizontal components of enstrophy also peak very close to the source. In contrast, the vertical component of enstrophy is linked to effects other than buoyancy (e.g., shear) and is driven by gradients in the horizontal velocity fluctuations. Consequently, vertical vorticity variances take longer to develop and reach their peaks further downstream, where interactions among these components intensify. It should be noted that in the stratified cases, the peak in enstrophy happens before the plume reaches the inversion height and it coincides with that of the neutral case. This indicates that the end of the initial phase and the start of the decay (mixing) phase of the plume development, is minimally influenced by the background stratification and is mainly controlled by the source characteristics and its mean buoyant flow. This is the stage where the transverse growth of the plume is limited (Fig. 11) and the TKE of the plume is large (Fig. 12).

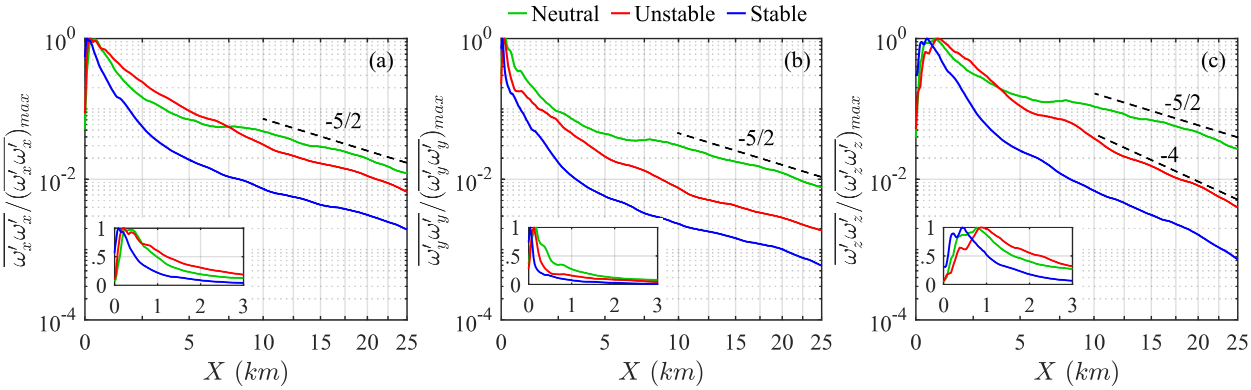

Fig. 13: Variation of the temporally and plume-averaged enstrophy components along the streamwise length: (a) streamwise enstrophy, (b) spanwise enstrophy, and (c) vertical enstrophy. The enstrophy components are normalized by their maximum values.

The different sloping trends of the plots in Fig. 13 suggest that the rate of decay in enstrophy components is different at different stages of plume development under different background conditions. After reaching their peak values, the enstrophy components in all cases decrease exponentially, but the decay rate varies among cases due to background conditions. The enstrophy decay is tied to how efficiently the plume exchanges energy with the surrounding flow primarily through entrainment of ambient air. Vortical structures, associated with regions of high enstrophy, enhance entrainment by creating strong local velocity gradients. These gradients pull in and mix surrounding fluid more effectively. The results in this section, therefore, can be connected to Figs. 11a and 11b, which illustrate the changes in the spanwise and vertical growth of the plume, reflecting the entrainment process.

Close to the heat source, the highest decay rate in $\overline{\omega_x'\omega_x'}$ is observed in the stable case with an exponent of -18.01, while the slowest decay occurs in the unstable case with an exponent of -8.2. This slower decay in the unstable case is attributed to the high mixing that leads to high spanwise entrainment (Fig 11a) and more energy in the vortical structures. In contrast, in the stable case, mixing is suppressed due to stratification, resulting in lower spanwise plume entrainment (Fig. 11a), and a steeper decay in the vortical energy.

The initial decay in $\overline{\omega_y'\omega_y'}$ is steeper than that of the streamwise enstrophy component, with decay exponents of -20.01 (neutral), -39.28 (unstable), and -57.87 (stable). The faster decay of the spanwise enstrophy component is attributed to different driving processes and is due to shear forces generated by the interaction between the plume and the incoming crosswind (manifested in the stretching term of the enstrophy budget; not shown). In the neutral case, these shear forces dominate, resulting in high vertical entrainments (Fig. 11b) and a slower decay of spanwise vorticity. In contrast, in the stratified cases, buoyancy effects from the background compete with shear forces, leading to a faster decay of spanwise enstrophy. Close to the heat source, the vertical enstrophy, $\overline{\omega_z'\omega_z'}$, decays with −8.56, −6.51, and −13.38 exponents for the neutral, unstable, and stable cases, respectively. This decay trend mirrors the behavior of decay observed for $\overline{\omega_x'\omega_x'}$, as both these components are influenced by the spanwise entrainment and growth of the plume (Fig. 11a). The slowest decay rate of $\overline{\omega_z'\omega_z'}$ in the unstable case is due to enhanced mixing, which leads to more effective maintenance of vertical vorticity and thus a slower decay in vortical energy.

Far from the source of buoyancy, all three components of enstrophy in the neutral case, as well as the horizontal enstrophy components of the stratified cases, exhibit an exponential decay with an exponent of approximately −5/2. This is in the region where the plumes in the stratified cases are well developed at the inversion height. The similar decaying behavior of $\overline{\omega_x'\omega_x'}$ and $\overline{\omega_y'\omega_y'}$ in the stable and unstable case plumes to the decaying behavior of the enstrophy components in the neutral case indicates that the mixing, cooling, and entrainment processes due to horizontal vorticities are unaffected by the stratification in the background flow. This similar behavior is also reflected in the vertical growth (and entrainment) of the plume across all three cases, where the plume expansion becomes constant in this region (Fig. 11b). However, the different decaying exponents of $\overline{\omega_z'\omega_z'}$ for the stable and unstable cases (i.e., −4 versus −5/2, Fig. 13c) suggest that the inversion height affects the development of vertical vorticities under stratified conditions.

To further understand the behavior of the enstrophy components and their contributions to the total rotational energy of the plume, the ratios between them were investigated in Fig. 14. In this figure, it can be seen that in the region close to the heat source and in the initial stage of plume development, the magnitude of the enstrophy components is very different (all three sub-plots). Specifically, in the region within the first 0.2 km from the source, the spanwise component is the largest, followed by the streamwise component. The dominance of the spanwise component in this region indicates that near the source, the xz-vortices generated by the interaction between the plume and the crosswind, have the largest contribution to the total vortical energy of the plume. In this near-source region, the magnitude of $\overline{\omega_y'\omega_y'}$ is, respectively, 4 – 10 times and 25 – 40 times larger than $\overline{\omega_x'\omega_x'}$ and $\overline{\omega_z'\omega_z'}$ across the three stability cases, with the differences being more pronounced in the case of unstable stratification. The dominance of $\overline{\omega_x'\omega_x'}$ over $\overline{\omega_z'\omega_z'}$ (Fig. 14b) near the source suggests that the buoyancy effect, represented by $\partial w'/\partial y$, is stronger than the mixing effects caused by horizontal shears, $\partial v'/\partial x$ and $\partial u'/\partial y$. After this near-source region, the effect of the horizontal crossflow starts to dominate over the buoyancy-driven rise from the heat source.

Far from the source, the ratios between any two enstrophy components in the neutral case asymptotically approach a value close to 1. This asymptote suggests that the components are influenced by similar mechanisms, such as vortex stretching, compression, and baroclinic torque, and the vortical fluctuations become isotropic. Such isotropy is missing in the stable and unstable cases far from the source. In these scenarios, the ratios between the streamwise and spanwise enstrophy components fluctuate slightly above unity (Fig. 14a), indicating that the flow structures in the yz-plane generally have higher energy compared to those in the xz-plane. In stratified cases, the ratios $\overline{\omega_x'\omega_x'},/\overline{\omega_z'\omega_z'}$ (Fig. 14b) and $\overline{\omega_y'\omega_y'}\ /\overline{\omega_z'\omega_z'}$ (Fig. 14c) increase after the plume reaches the inversion layer due to a steep decrease in vertical enstrophy ($\overline{\omega_z'\omega_z'}$). This drop occurs because vertical mixing is limited in the inversion layer, which enhances horizontal diffusion and vortex shedding and breakup in both these scenarios.

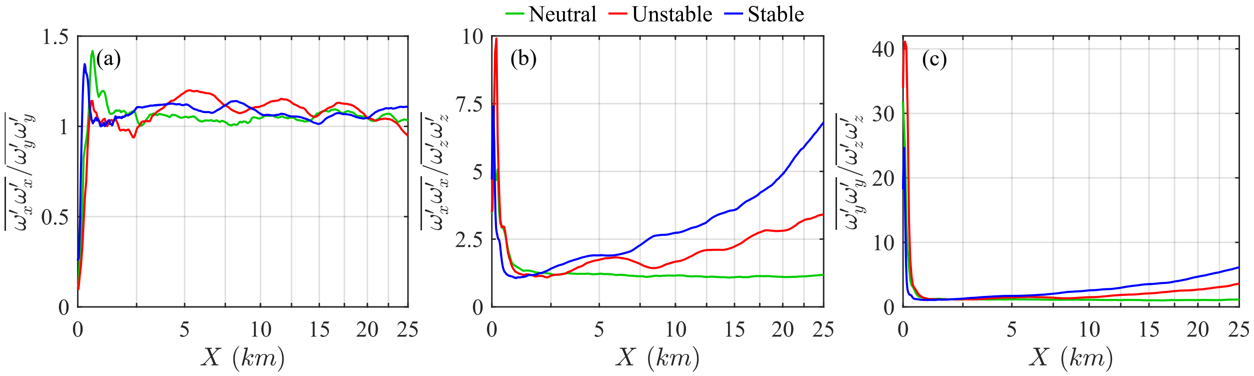

Fig. 14: Ratio of temporally and plume-averaged enstrophy components along the horizontal direction.

4. Summary and Conclusion

Atmospheric stratification plays an important role in shaping plume dynamics, particularly in terms of energy distribution, propagation velocity, mixing, and scalar dispersion. This study used large eddy simulations to investigate how diurnal variations in atmospheric stability affect a turbulent buoyant plume in crossflow.

The results highlighted the critical role of atmospheric stratification on plume behavior. Key characteristics, such as plume rise, angle, and shape are all influenced by the ambient stratification. Under neutral conditions, the plume rise is primarily governed by the shear and buoyancy of the heat source. However, in stratified cases, the plume's behavior is further affected by the background buoyancy and inversion layer. Under the stable nighttime condition, the plume exhibited the highest scalar density at lower elevations, with low-level jets interacting with the plume and carrying scalars downstream while restricting mixing. In contrast, the unstable daytime condition enhanced mixing and lateral dispersion, producing a broader, more laterally dispersed plume that travels at greater heights and higher velocities compared to the nighttime. These results indicate that nighttime plumes, with their higher density and lower-level travel path, can pose greater concerns for nearby communities compared to daytime plumes.

Near the source, the plume's centerline properties were primarily governed by the source buoyancy. However, as the distance from the source increased, the influence of atmospheric stratification became increasingly significant across all cases. Further from the heat source, the plume exhibited isotropic behavior in the neutral scenario. However, in the stratified cases, the inversion layer prevented the development of isotropy. The plume entrainment, mixing, and energy content were also strongly influenced by atmospheric stability.

These findings have important implications for applications like prescribed burn planning and urban pollution control. For instance, they can help fire managers better understand short- and long-range smoke transport during controlled burns, ensuring that smoke does not impact nearby communities or sensitive ecosystems. By considering the significant variations in plume behavior under different atmospheric stratification conditions, practitioners can make more informed decisions to minimize the harmful effects of pollutants on both ecosystems and communities.

Acknowledgment

This work is supported by funding from the Department of Defense Strategic Environmental Research and Development Program (SERDP) grant number RC20-1298 and National Science Foundation (NSF) grant number CBET 2043103. In addition, this research used resources from the National Energy Research Scientific Computing Center, a DOE Office of Science User Facility supported by the Office of Science of the U.S. Department of Energy under Contract No. DE-AC02-05CH11231 using NERSC award BER-ERCAP0022408. We would also like to acknowledge high-performance computing support from Cheyenne (doi:10.5065/D6RX99HX) provided by NCAR's Computational and Information Systems Laboratory, sponsored by the National Science Foundation. We also thank the FSU Research and Computing Center for providing additional computing resources.

Appendix A: Grid sensitivity analysis

Figure 15 illustrates the variation of time and horizontally averaged profiles of streamwise velocity, potential temperature, and resolution ratio (γ) across various grid sizes for the unstable case. The stable and neutral cases exhibit similar patterns of variation.

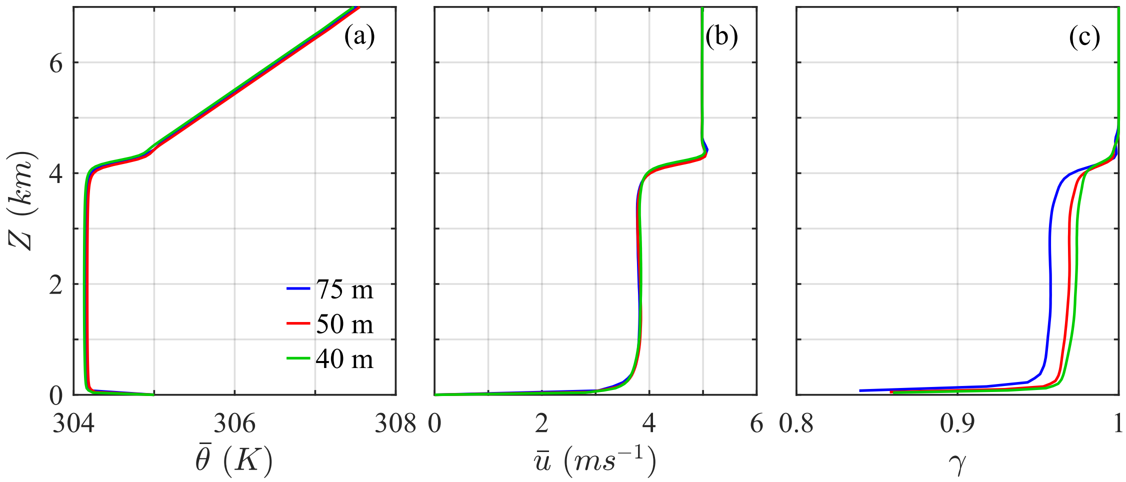

Fig. 15: Temporally and horizontally averaged vertical profiles of (a) potential temperature, (b) streamwise velocity, and (c) resolution ratio for the unstable case.

Reducing the grid size from 75 m to 40 m caused a maximum change of 6.2% in the mean streamwise velocity for the neutral case and 2.6% for the unstable case. In contrast, for the stable case, this reduction led to a substantial 20% change, which decreased to 9% when the grid size was further refined to 25 m. The percentage change in the potential temperature was less pronounced than that of the streamwise velocity across all cases.

The maximum change in the resolution ratio was observed to be 2.3% and 3.1% for the unstable and neutral cases, respectively, when the grid size decreased from 75 m to 50 m. This difference, respectively, reduced to 0.2% and 2.3% for these cases as the grid size was further reduced to 40 m. A similar trend was observed for the friction velocity, supporting the selection of a 50 m grid size as adequate for both the neutral and unstable cases. For the stable case, the grid size was successively reduced from 75 m to 50 m, then to 40 m, and finally to 25 m. The largest change in resolution ratio occurred when the grid size was reduced from 75 m to 50 m (25.34%), but the change became smaller as the grid size decreased further, with only a 9.13% change when going from 40 m to 25 m, making the 25 m grid size the most suitable choice for this scenario. Similar trends were observed in the friction velocity for the stable case.

Appendix B: Time averaged normalized potential temperature contours

Figure 16 shows normalized profiles of potential temperature ($\overline{\theta_n}$) for the three cases. The normalized potential temperature was calculated based on $\overline{\theta_n} = (\bar{\theta} - \overline{\theta_0})/\overline{\theta_0}$, where $\bar{\theta}$ represents the time-averaged potential temperature over 1800 s, and $\overline{\theta_0}$ is the time and spatially averaged potential temperature prior to the initiation of the source heat flux. In the stratified cases, spatial averaging was conducted below the inversion layer, yielding $\overline{\theta_0}$ values of 304.36 K and 294.46 K for the unstable and stable cases, respectively, while this value is 300 K for the neutral case across the entire domain.

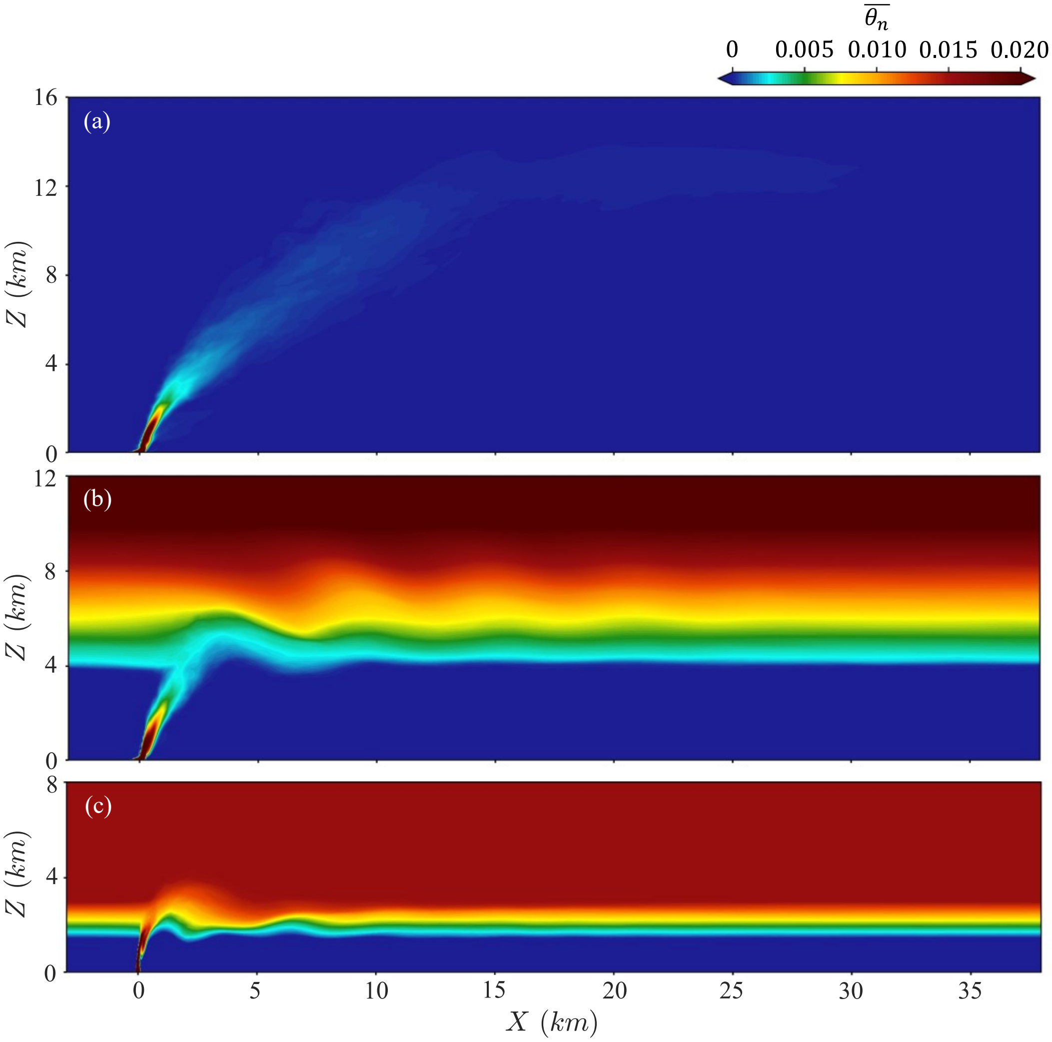

Fig. 16: Vertical cross-sections of the time-averaged normalized potential temperature contours at the middle of the domain under different stratification conditions: (a) neutral, (b) unstable, and (c) stable. The plume was averaged over a duration of 1800 s.

References

Andreae, M. O., Rosenfeld, D., Artaxo, P., Costa, A. A., Frank, G., Longo, K. M., & Silva-Dias, M. A. F. da. (2004). Smoking rain clouds over the Amazon. *Science*, *303*(5662), 1337–1342.

Ardeshiri, H., Cassiani, M., Park, S. Y., Stohl, A., Pisso, I., & Dinger, A. S. (2020). On the convergence and capability of the large-eddy simulation of concentration fluctuations in passive plumes for a neutral boundary layer at infinite Reynolds number. *Boundary-Layer Meteorology*, *176*, 291–327.

Ashrafi, K., Orkomi, A. A., & Motlagh, M. S. (2017). Direct effect of atmospheric turbulence on plume rise in a neutral atmosphere. *Atmospheric Pollution Research*, *8*(4), 640–651.

Bhaganagar, K., & Bhimireddy, S. R. (2020). Numerical investigation of starting turbulent buoyant plumes released in neutral atmosphere. *Journal of Fluid Mechanics*, *900*, A32.

Blackadar, A. K. (1957). Boundary layer wind maxima and their significance for the growth of nocturnal inversions. *Bulletin of the American Meteorological Society*, *38*(5), 283–290.

Breton, S.-P., Sumner, J., Sørensen, J. N., Hansen, K. S., Sarmast, S., & Ivanell, S. (2017). A survey of modelling methods for high-fidelity wind farm simulations using large eddy simulation. *Philosophical Transactions of the Royal Society A: Mathematical, Physical and Engineering Sciences*, *375*(2091), 20160097.

Briggs, G. A. (1972). Chimney plumes in neutral and stable surroundings. *Atmospheric Environment (1967)*, *6*(7), 507–510.

Carey, S., & Bursik, M. (2015). Volcanic plumes. In *The encyclopedia of volcanoes* (pp. 571–585). Elsevier.

Chen, C. H., & Bhaganagar, K. (2023). Energetics of buoyancy-generated turbulent flows with active scalar: Pure buoyant plume. *Journal of Fluid Mechanics*, *954*, A23.

Chung, H., & Koseff, J. R. (2023). Interaction of a buoyant plume with a turbulent canopy mixing layer. *Physical Review Fluids*, *8*(6), 064501.

Church, C. R., Snow, J. T., & Dessens, J. (1980). Intense atmospheric vortices associated with a 1000 MW fire. *Bulletin of the American Meteorological Society*, *61*(7), 682–694.

Contini, D., Cesari, D., Donateo, A., & Robins, A. (2009). Effects of Reynolds number on stack plume trajectories simulated with small scale models in a wind tunnel. *Journal of Wind Engineering and Industrial Aerodynamics*, *97*(9–10), 468–474.

Cortelezzi, L., & Karagozian, A. R. (2001). On the formation of the counter-rotating vortex pair in transverse jets. *Journal of Fluid Mechanics*, *446*, 347–373.

Cunningham, P., Goodrick, S. L., Hussaini, M. Y., & Linn, R. R. (2005). Coherent vortical structures in numerical simulations of buoyant plumes from wildland fires. *International Journal of Wildland Fire*, *14*(1), 61–75.

Deardorff, J. W. (1980). Stratocumulus-capped mixed layers derived from a three-dimensional model. *Boundary-Layer Meteorology*, *18*, 495–527.

Devenish, B., Rooney, G., & Thomson, D. (2010). Large-eddy simulation of a buoyant plume in uniform and stably stratified environments. *Journal of Fluid Mechanics*, *652*, 75–103.

Dey, S., Mallen, E., Stone Jr, B., & Joshi, Y. (2023). Evaluation and Validation of Microscale Atmospheric Modeling With Offline Weather Research and Forecasting Model to Parallelized Large-Eddy Simulation Model Forcing Conditions. *Journal of Engineering for Sustainable Buildings and Cities*, *4*(1), 011003.

Diez, F., Sangras, R., Faeth, G., & Kwon, O. (2003). Self-preserving properties of unsteady round buoyant turbulent plumes and thermals in still fluids. *J. Heat Transfer*, *125*(5), 821–830.

Duan, G., Jackson, J., & Ngan, K. (2019). Scalar mixing in an urban canyon. *Environmental Fluid Mechanics*, *19*, 911–939.

Duan, G., & Ngan, K. (2019). Sensitivity of turbulent flow around a 3-D building array to urban boundary-layer stability. *Journal of Wind Engineering and Industrial Aerodynamics*, *193*, 103958.

Ellison, T., & Turner, J. (1959). Turbulent entrainment in stratified flows. *Journal of Fluid Mechanics*, *6*(3), 423–448.

Ezzamel, A., Salizzoni, P., & Hunt, G. R. (2015). Dynamical variability of axisymmetric buoyant plumes. *Journal of Fluid Mechanics*, *765*, 576–611.

Finney, M. A., McAllister, S. S., Forthofer, J. M., & Grumstrup, T. P. (2021). *Wildland fire behaviour: Dynamics, principles and processes*. CSIRO publishing.

Fric, T., & Roshko, A. (1994). Vortical structure in the wake of a transverse jet. *Journal of Fluid Mechanics*, *279*, 1–47.

Golay, M. W. (1982). Numerical modeling of buoyant plumes in a turbulent, stratified atmosphere. *Atmospheric Environment (1967)*, *16*(10), 2373–2381.

Gronemeier, T., Surm, K., Harms, F., Leitl, B., Maronga, B., & Raasch, S. (2021). Evaluation of the dynamic core of the PALM model system 6.0 in a neutrally stratified urban environment: Comparison between LES and wind-tunnel experiments. *Geoscientific Model Development*, *14*(6), 3317–3333.

Hewitt, I. J. (2020). Subglacial plumes. *Annual Review of Fluid Mechanics*, *52*(1), 145–169.

Huq, P. (1997). Observations of jets in density stratified crossflows. *Atmospheric Environment*, *31*(13), 2011–2022.

Jordan, O. H., Rooney, G. G., Devenish, B. J., & van Reeuwijk, M. (2022). Under pressure: Turbulent plumes in a uniform crossflow. *Journal of Fluid Mechanics*, *932*, A47.

Khan, J. ul R., & Rao, S. (2023). Entrainment and bulk flow characteristics of heated and unheated transient plumes using direct numerical simulations. *Physics of Fluids*, *35*(12).

Lareau, N., & Clements, C. (2015). Cold smoke: Smoke-induced density currents cause unexpected smoke transport near large wildfires. *Atmospheric Chemistry and Physics*, *15*(20), 11513–11520.

Larsen, A. E., Reich, B. J., Ruminski, M., & Rappold, A. G. (2018). Impacts of fire smoke plumes on regional air quality, 2006–2013. *Journal of Exposure Science & Environmental Epidemiology*, *28*(4), 319–327.

Lo, K., & Ngan, K. (2015). Characterising the pollutant ventilation characteristics of street canyons using the tracer age and age spectrum. *Atmospheric Environment*, *122*, 611–621.

Lotrecchiano, N., Sofia, D., Giuliano, A., Barletta, D., Poletto, M., & others. (2020). Pollution dispersion from a fire using a Gaussian plume model. *Int. J. Saf. Secur. Eng*, *10*, 431–439.

Mahesh, K. (2013). The interaction of jets with crossflow. *Annual Review of Fluid Mechanics*, *45*(1), 379–407.

Mahrt, L. (1998). Stratified atmospheric boundary layers and breakdown of models. *Theoretical and Computational Fluid Dynamics*, *11*(3), 263–279.

Mallia, D. V., & Kochanski, A. K. (2023). A review of modeling approaches used to simulate smoke transport and dispersion. *Landscape Fire, Smoke, and Health: Linking Biomass Burning Emissions to Human Well-Being*, 127–148.

Maronga, B. (2014). Monin–Obukhov similarity functions for the structure parameters of temperature and humidity in the unstable surface layer: Results from high-resolution large-eddy simulations. *Journal of the Atmospheric Sciences*, *71*(2), 716–733.

Maronga, B., Banzhaf, S., Burmeister, C., Esch, T., Forkel, R., Fröhlich, D., Fuka, V., Gehrke, K. F., Geletič, J., Giersch, S., & others. (2020). Overview of the PALM model system 6.0. *Geoscientific Model Development*, *13*(3), 1335–1372.

Maronga, B., Gryschka, M., Heinze, R., Hoffmann, F., Kanani-Sühring, F., Keck, M., Ketelsen, K., Letzel, M. O., Sühring, M., & Raasch, S. (2015). The Parallelized Large-Eddy Simulation Model (PALM) version 4.0 for atmospheric and oceanic flows: Model formulation, recent developments, and future perspectives. *Geoscientific Model Development*, *8*(8), 2515–2551.

Matulka, A., López, P., Redondo, J., & Tarquis, A. (2014). On the entrainment coefficient in a forced plume: Quantitative effects of source parameters. *Nonlinear Processes in Geophysics*, *21*(1), 269–278.

Meehan, M. A., & Hamlington, P. E. (2023). Richardson and Reynolds number effects on the near field of buoyant plumes: Flow statistics and fluxes. *Journal of Fluid Mechanics*, *961*, A7.

Mirajkar, H. N., & Balasubramanian, S. (2017). Effects of varying ambient stratification strengths on the dynamics of a turbulent buoyant plume. *Journal of Hydraulic Engineering*, *143*(7), 04017013.

Moeng, C.-H., & Sullivan, P. P. (1994). A comparison of shear-and buoyancy-driven planetary boundary layer flows. *Journal of Atmospheric Sciences*, *51*(7), 999–1022.

Morton, B. R., Taylor, G. I., & Turner, J. S. (1956). Turbulent gravitational convection from maintained and instantaneous sources. *Proceedings of the Royal Society of London. Series A. Mathematical and Physical Sciences*, *234*(1196), 1–23.

Mukherjee, P., Mirajkar, H. N., & Balasubramanian, S. (2023). Entrainment dynamics of buoyant jets in a stably stratified environment. *Environmental Fluid Mechanics*, *23*(5), 1051–1073.

Nakayama, H., Takemi, T., & Nagai, H. (2014). Large-eddy simulation of plume dispersion under various thermally stratified boundary layers. *Advances in Science and Research*, *11*(1), 75–81.

Paleri, S., Wanner, L., Sühring, M., Desai, A., & Mauder, M. (2023). Coupled large eddy simulations of land surface heterogeneity effects and diurnal evolution of late summer and early autumn atmospheric boundary layers during the CHEESEHEAD19 field campaign. *EGUsphere*, *2023*, 1–43.

Park, S.-B., Baik, J.-J., Raasch, S., & Letzel, M. O. (2012). A large-eddy simulation study of thermal effects on turbulent flow and dispersion in and above a street canyon. *Journal of Applied Meteorology and Climatology*, *51*(5), 829–841.

Park, S.-B., Baik, J.-J., & Ryu, Y.-H. (2013). A large-eddy simulation study of bottom-heating effects on scalar dispersion in and above a cubical building array. *Journal of Applied Meteorology and Climatology*, *52*(8), 1738–1752.

Penner, J. E., Dickinson, R. E., & O'Neill, C. A. (1992). Effects of aerosol from biomass burning on the global radiation budget. *Science*, *256*(5062), 1432–1434.

Pham, M., Plourde, F., & Doan, K. (2007). Direct and large-eddy simulations of a pure thermal plume. *Physics of Fluids*, *19*(12).

Pham, M. V., Plourde, F. D. R., & Kim, S. D. (2005). Three-dimensional characterization of a pure thermal plume. *J. Heat Transfer*, *127*(6), 624–636.

Potter, B. E. (2012). Atmospheric interactions with wildland fire behaviour–II. Plume and vortex dynamics. *International Journal of Wildland Fire*, *21*(7), 802–817.

Price, O. F., Horsey, B., & Jiang, N. (2016). Local and regional smoke impacts from prescribed fires. *Natural Hazards and Earth System Sciences*, *16*(10), 2247–2257.

Priestley, C., & Ball, F. (1955). Continuous convection from an isolated source of heat. *Quarterly Journal of the Royal Meteorological Society*, *81*(348), 144–157.

Raasch, S., & Etling, D. (1991). Numerical simulation of rotating turbulent thermal convection. *Contributions to Atmospheric Physics*, *64*(3), 185–199.

Robock, A. (1988). Enhancement of surface cooling due to forest fire smoke. *Science*, *242*(4880), 911–913.

Scase, M., Caulfield, C., & Dalziel, S. (2006). Boussinesq plumes and jets with decreasing source strengths in stratified environments. *Journal of Fluid Mechanics*, *563*, 463–472.

Slawson, P., & Csanady, G. (1971). The effect of atmospheric conditions on plume rise. *Journal of Fluid Mechanics*, *47*(1), 33–49.

Stull, R. B. (2012). *An introduction to boundary layer meteorology* (Vol. 13). Springer Science & Business Media.

Turner, J. (1962). The 'starting plume'in neutral surroundings. *Journal of Fluid Mechanics*, *13*(3), 356–368.

Turner, J. (1969). Buoyant plumes and thermals. *Annual Review of Fluid Mechanics*, *1*(1), 29–44.

Uyanwaththa, A., Malalasekera, W., Hargrave, G., & Dubal, M. (2019). Large eddy simulation of scalar mixing in jet in a cross-flow. *Journal of Engineering for Gas Turbines and Power*, *141*(6), 061005.

Wei, W., Zhang, H., Zhang, X., & Che, H. (2023). Low-level jets and their implications on air pollution: A review. *Frontiers in Environmental Science*, *10*, 1082623.

Wicker, L. J., & Skamarock, W. C. (2002). Time-splitting methods for elastic models using forward time schemes. *Monthly Weather Review*, *130*(8), 2088–2097.

Williamson, J. H. (1980). Low-storage runge-kutta schemes. *Journal of Computational Physics*, *35*(1), 48–56.

Wright, S. J. (1994). The effect of ambient turbulence on jet mixing. In *Recent research advances in the fluid mechanics of turbulent jets and plumes* (pp. 13–27). Springer.

Wurps, H., Steinfeld, G., & Heinz, S. (2020). Grid-resolution requirements for large-eddy simulations of the atmospheric boundary layer. *Boundary-Layer Meteorology*, *175*(2), 179–201.

Yaghoobian, N., Kleissl, J., & Paw U, K. T. (2014). An improved three-dimensional simulation of the diurnally varying street-canyon flow. *Boundary-Layer Meteorology*, *153*, 251–276.